JOURNAL OF AIRCRAFT
Vol. 46, No. 2, March–April 2009

Reynolds-Averaged Navier–Stokes Solutions for the CAWAPI F-16XL Using Different Hybrid Grids

Willy Fritz*
European Aeronautic Defence and Space (EADS) Military Air Systems, 81663 Munich, Germany
M. Bruce Davis†
Lockheed Martin Aeronautics Company, Fort Worth, Texas 76101
Steve L. Karman Jr.‡
University of Tennessee, Chattanooga, Tennessee 37403
and
Todd Michal§
The Boeing Company, St. Louis, Missouri 63166

DOI: 10.2514/1.35106

Ten groups participating in the Cranked Arrow Wing Aerodynamics Project International (CAWAPI) within the NATO-RTO task group AVT 113 have contributed viscous simulations of a full scale model of the F-16XL aircraft at different flight conditions. Three different classes of grids have been used by the different participants: a common structured grid, a common unstructured grid, and so-called individually tailored grids, which have been used by four participants: Lockheed Martin Aeronautics Company, University of Tennessee, Boeing Phantom Works, and EADS Military Air Systems. This paper focuses on the use of these individually generated grids. The different grid generation techniques and strategies (nonadapted, manually adapted, and solution-based adapted) are discussed and the solutions obtained in these individually tuned grids are compared with flight test data for different test cases.

Nomenclature

C_f = local skin friction coefficient
C_p = pressure coefficient
M = abbreviation for “million”
M_∞ = freestream Mach number
v/v_e = ratio of velocity magnitude in boundary layer to that at the rake extreme total-pressure tube
x/c_{local} = fractional distance along the local chord, positive aft
$y+$ = dimensionless sublayer scale, $u_\tau y/\nu$
$2y/b_{\text{local}}$ = fractional distance along the local semispan, positive toward the right wing tip

I. Introduction

THE participation in the Cranked Arrow Wing Aerodynamics Project International (CAWAPI) [1] with the flight test database of the F-16XL aircraft [2] was an excellent opportunity for all participants to validate and assess their computational fluid dynamics (CFD) tools with respect to accuracy and computational effort. Validation could be done not only by comparison with flight test data, but also by comparison of numerical results obtained by different codes. Three different classes of grids have been used by the ten different participants [3]: a common structured grid, which was generated by the National Aerospace Laboratory, The Netherlands (NLR) [used by NLR [4], the University of Liverpool, United Kingdom [5], and NASA [6]], a common unstructured, hybrid grid which was generated by the U.S. Air Force Academy (USAFA) (used by the Swedish Defence Research Agency and the Royal Institute of Technology, Sweden [7], NASA [8], and the USAFA [9]), and finally the so-called “individually tailored” grids [used by Boeing [10], the European Aeronautic Defence and Space Company–Military Air Systems (EADS–MAS) [11], the Lockheed Martin Aeronautics Company (LM Aero) [12], and the University of Tennessee at Chattanooga (UTSimC) [13]].

The reason for the latter four participants using such “tailored” grids was to get experience and guidelines in generating, refining, and adapting grids for such a complex configuration, as in industrial work grid generation is a substantial requisite for a successful CFD simulation. This paper reports on the CFD simulations using those individually tailored grids.

II. Geometry

A detailed description of the aircraft geometry is given in [2,3]. Figure 1 shows the CAWAPI F-16XL in flight (Fig. 1a) and the resulting surface geometry as it was used for the grid generation within the present study.

As can be seen in Fig. 1b, all essential details of the geometry (air dam, actuator pod, wing tip missile with rail) have been included into the numerical model. A further important detail of the geometry is the shape of the leading edge. At the apex (position 1 in Fig. 1), the wing starts with a cropped sharp leading edge, which merges with a round leading edge (position 2). At position 3 there is again a transition toward a sharp leading edge and the outer part of the wing finally has a sharp leading edge. Modeling these leading-edge details is crucial for accurate viscous flow simulations.

III. Test Cases

Seven different flight conditions (FC) have been selected from the flight test database [1,2] for the use in the RTO-AVT-113 task group. This paper will focus on results for four of those test cases, which have also been calculated by all the other members of the task group [4–13]. They are shown in Table 1.

Received 12 October 2007; revision received 17 November 2008; accepted for publication 17 November 2008.

*Research and Development Engineer, Aerodynamics and Methods; willy.fritz@eads.com. Senior Member AIAA.

†Aerospace Engineer, Aerodynamics and Computational Fluid Dynamics; myron.b.davis@lmco.com. Member AIAA.

‡Research Professor, Graduate School of Computational Engineering; Steve-Karman@utc.edu. Associate Fellow AIAA.

§Phantom Works, Technical Fellow; todd.r.michal@boeing.com. Associate Fellow AIAA.

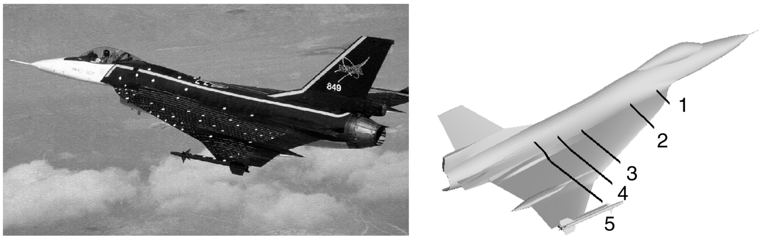

a) F - 16XL in flight

b) Geometry used in CFD simulations

Fig. 1 F-16XL geometry.

For all of the previous flight conditions, a sideslip angle of 0 deg was assumed, and thus they were calculated as symmetric. FC 7 was chosen because boundary-layer data (velocity profiles) from flight tests were available and FC 19 was selected because there is surface skin friction data. FC 25 has the highest angle of attack. These three flight conditions should all have a vortical flowfield. Finally FC 70 is a transonic test case with a very low angle of attack.

IV. Grid Generation

The grids used in this study can be split up into three categories: manually adapted grids (UT SimC, LM Aero), adaptation to solution features (Boeing), and solution-based adapted grids (EADS). A detailed description of the generation of the grids for this study is given by Boelens et al. in [3] and in the individual AIAA papers of the authors [10–13]. Thus only the essential parts of the grid generation are described in the following section.

A. Grid Generation at UT SimC

The grid at UT SimC was generated in two steps: first an inviscid unstructured mesh was generated and then viscous layers were added to this inviscid mesh [3].

Flow solutions at UTSimC with this grid have shown mostly good results compared with the available flight test data. However, in many of the cases the comparisons at the outboard span stations did not agree well with the flight test data. The suction peaks were too close to the wing leading edge. An investigation of the physical modeling by use of the various turbulence models [Spalart–Allmaras (SA), Menter–SAS (scale adaptive simulation), shear stress transport (SST) k–ω, and SST-DES (detached eddy simulation)] has shown no significant improvement (more details are given in [13]). It appeared as though the leading-edge vortex was traveling more outboard than the data showed, so the mesh resolution in the vicinity of the expected trajectory of the vortex was increased. This mesh adaptation was performed manually within the described meshing process and did not involve any solution-based grid adaptation.

B. Grid Generation at LM Aero

The grid which was generated at UT SimC was also provided to LM Aero with a notable exception. The original UT SimC grid fully resolved the turbulent boundary layer, whereas wall functions were used in all simulations at LM Aero and hence the boundary layer was less well resolved, especially in the viscous sublayer. The boundary-layer mesh at UT SimC has an initial spacing of 3×10^{-6} ($y^+ = 1$), whereas the LM Aero mesh has an initial spacing of 5×10^{-5} ($y^+ = 6$). The number of cell layers inserted into the UT SimC mesh is 27 at most, while it is 20 at most for the LM Aero mesh. The two grids started with the same inviscid mesh, so it is expected that outside of the boundary layer the grids are identical or very similar.

C. Grid Generation at Boeing Phantom Works

Boeing began its participation in the CAWAPI effort by generating CFD solutions on the common unstructured grid supplied to all CAWAPI team members. A complete description of this grid is given in [3]. Boeing's predictions on the common grid were consistent with the results shown by other CAWAPI participants; however, several important flowfield details were not accurately predicted on this grid. In particular, the strength of the secondary vortex was significantly underpredicted. Several new grids were generated at Boeing to investigate the impact of grid resolution and cell topology on solution accuracy.

A new baseline mesh with higher resolution in the wing leading-edge region was constructed at Boeing [3]. The resolution of this baseline Boeing surface mesh is about double that of the common mesh in the immediate proximity of the wing vortices.

To help assess the impact of the off body grid resolution, several new volume meshes were created with increased resolution along the vortex core paths. The new meshes were adapted by placing grid resolution sources along traces of the primary vortex paths predicted in the baseline mesh solutions. The adapted grids used the same surface grid as the baseline Boeing grid, but the addition of sources increased the size of the volume grid. More details on the grid adaptation approach are given in [10].

D. Grid Generation at EADS–MAS

As it was unknown whether a common unstructured grid could be used by all participants (due to specific requirements of the different flow solvers) and because a systematic grid refinement study was planned, EADS–MAS decided to generate its own hybrid grid right from the beginning. First grids have been generated with the commercial hybrid grid generator from “CentaurSoft,”[¶] applying a user controlled clustering for a priori adaptation of the grid to the expected vortical flow structure.

Flow calculations with such “manually adapted” grids were not very satisfactory. Specifically, for the test cases with vortical flow structure, the leeward suction peaks due to the leading-edge vortices were underpredicted and finer grids with up to 22 million grid points were no guarantor for proper flow solutions. So it was clear, that the point distribution in the field was not always optimal. To overcome this problem, the solution-based grid adaptation which is included in the German Aerospace Center (DLR) TAU code [14–16] was used for all further calculations [3,11].

E. Final Grid Sizes

The manually adapted grid which was used by UT SimC for all test cases contained 13,906,674 points, 32,395,936 tetrahedra, 166,230 pyramids, 15,770,674 prisms, and 352,656 hexahedra. The grid used by LM Aero is very similar to that grid; the only significant difference is the number of prisms and hexahedral cells, which are used to grow the viscous mesh from the boundary layer. So the final LM Aero mesh consisted of 32,415,471 tetrahedral cells, 9,612,208 prisms, 212,400 hexahedral cells, and 188,175 pyramids.

The new baseline Boeing surface mesh resulted in a volume grid having 13.3 million cells. By the additional increased grid resolution along the vortex paths, the size of the volume grid was increased by an additional 4 million cells.

Within the solution-based grid adaptation of EADS–MAS an individual grid for each flow condition was used. Starting from a common initial grid with 10 million nodes the final grid for each test case was obtained by four adaptation steps. The final grid sizes were between 19 million and 22 million grid points.

[¶] CentaurSoft Grid Generator, data available online at http://www.centaursoft.com [retrieved 26 September 2007].

Table 1 Calculated flight conditions

Flight condition	Actual Mach no.	Actual α, deg	Actual β, deg	Actual Reynolds no.
FC 7	0.304	11.89	−0.133	44.4E + 06
FC 19	0.36	11.85	+0.612	44.8E + 06
FC 25	0.242	19.84	+0.725	32.22E + 06
FC 70	0.97	4.37	+0.310	88.77E + 06

All the given grid sizes are for the half-model of the F-16XL, respectively.

V. Flow Solution

A. Flow Solver Used at LM Aero

The LM Aero flow-solver Falcon is a finite-volume CFD system that has been developed and maintained by the LM Aero Aerodynamics and CFD Branch. The latest, improved version, Falcon v4, has the capability to use multiple element grid types, such as hybrid grids with a variety of cell shapes.

The governing equations in the Falcon v4 solver are the compressible Reynolds-averaged Navier–Stokes (RANS) equations. A steady-state solution to the governing equations is obtained by using an implicit time marching scheme with upwind differenced fluxes for the inviscid terms and central differenced fluxes for the viscous terms. Inviscid fluxes are computed using Roe's approximate Riemann solver [17]. The primitive variables (ρ, u, v, w, and T) are extrapolated to the face for higher order accuracy. Viscous fluxes are computed from gradient estimates at the cell faces. The face gradients are calculated as the distance weighted average of the gradients at the centroids of the two cells on either side of the face. The component normal to the interface is then replaced with the local information. The Falcon code includes the two-equation k–kl turbulence model by Smith [18] (with an algebraic stress model option) for accurate turbulence calculations. For unsteady calculations, a large eddy simulation (LES) model can be used. A wall-layer model (or wall function) is generally used to reduce the number of points required for accurate boundary-layer calculations.

A highly implicit numerical solver has been implemented using incomplete lower–upper factorization. The implicit Jacobians are stored such that they do not need to be calculated at each time step. This variable update of the Jacobians significantly reduces CPU time. All of the boundary conditions are applied/computed implicitly. The code also includes the capability to accurately solve very low-speed and mixed speed flows using low-speed preconditioning [19]. The code can be run with any of several different gas models. These include constant gamma, variable gamma as a function of temperature for air, variable gamma for a typical jet engine exhaust, or a four species flow model.

Although the code uses nondimensional values internally, inputs to the code and outputs from the code can be in either English or SI units. The code can perform accurate unsteady (time-accurate) analyses using subiterations. Falcon v4 is set up to efficiently perform on a parallel computer using the standard message passing interface (MPI), with domain decomposition produced by the METIS algorithm [20]. For restart files, grids, and boundary condition specifications, the code uses an enhanced, self-describing, platform independent file system to facilitate working on a heterogeneous computer network. More details are given in [12].

B. Flow Solver Used at UT SimC

The UT SimC flowfield solution algorithm is related to several previous efforts and has evolved over more than 15 years of development. The approach is an evolution of the implicit flow solver and code of Anderson et al. [21–23]. The solver developed in these references demonstrated accurate 3-D, implicit, high Reynolds number solution capability. The parallel version of the unstructured algorithm is detailed in Hyams et al. [24]. Brief descriptions of some of the aspects of the flow solver are described next.

Arbitrary Mach Algorithm: The staple of the structured and unstructured SimCenter flow solution code is an algorithm well suited for simulation of both high-speed and low-speed flows. This formulation was presented by Briley et al. and is termed the arbitrary Mach number algorithm, which is a preconditioned Roe flux-difference formulation for nondimensional primitive variables [25].

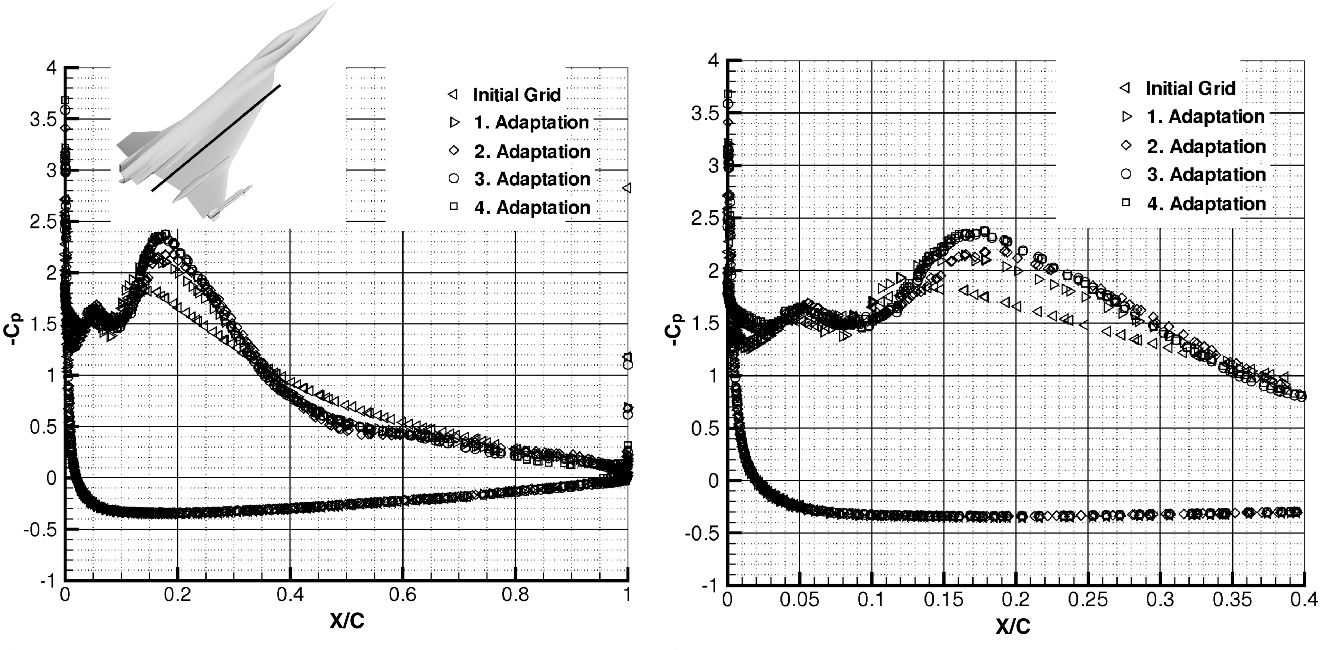

a) BL 70

b) BL 70 Close up at leading edge

Fig. 2 Influence of grid adaptation on C_p for FC 25 ($M_\infty = 0.242$, $\alpha = 19.8$ deg, and $Re = 32.22$ M) at butt line 70.

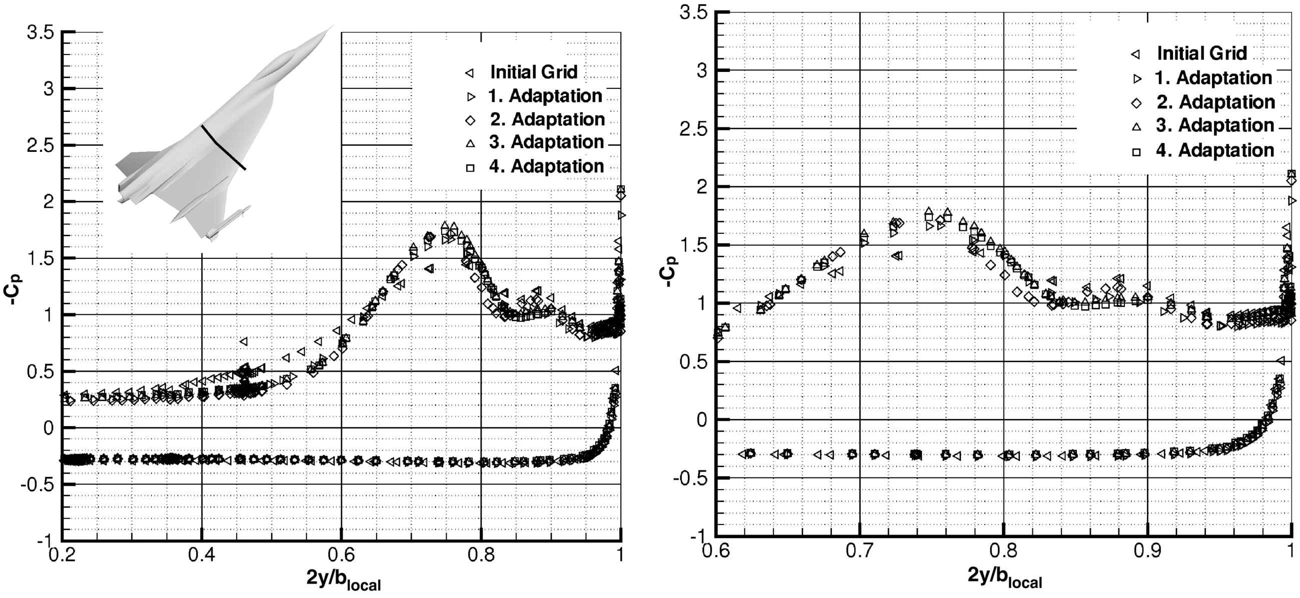

a) FS 337.5

b) FS 337.5 Close up at wing tip

Fig. 3 Influence of grid adaptation on C_p for FC 25 ($M_\infty = 0.242$, $\alpha = 19.8$ deg, and $Re = 32.22$ M) at fuselage station 337.5.

The unsteady, three-dimensional, compressible, Reynolds-averaged Navier–Stokes equations are in Cartesian coordinates and in conservative form. The solution variables are expressed in their primitive form in the arbitrary Mach number algorithm: The arbitrary Mach algorithm depends on a simple, single-parameter diagonal matrix for conditioning of the system matrix eigenvalues. This leads to a low-cost implementation of the algorithm that is an effective convergence accelerator that converges favorably regardless of the local flow speed. Thus, simulation domains that contain regions of high-speed and low-speed flow are particularly well treated by this algorithm. The algorithmic approach has been validated for a range of problems, from simple to complex geometries and from low- ($M_\infty = 0.001$, incompressible) to high- (supersonic) speed flows [25]. Above $M_\infty = 1$, this algorithm behaves exactly as a conservative compressible flow solver with solution variables in the primitive form.

Iteration Hierarchy: The time evolution algorithm uses Newton iterations to remove time linearization errors in the unsteady terms. The time evolution algorithm is implicit, such that a linear system of equations is solved at each Newton iteration. The solution of the linear system is obtained via a symmetric Gauss–Seidel algorithm (point relaxation) that has been used successfully and extensively [24].

Parallel Solver: The parallel solution procedure consists of a scalable solution algorithm implemented to run efficiently on grid subdomains distributed across multiple processors and communicating through MPI. The algorithm has multiple nested kernels, viz., time step, Newton iteration, the lower–upper symmetric Gauss–Seidel (LU/SGS) iteration, etc., and the subdomain coupling is at the innermost level, that is, in the solution of the linear system. A block-Jacobi–type updating of the subdomain boundaries ensures efficient parallelization with a small incremental cost incurred in terms of subiterations required to recover the convergence rate of the sequential algorithm. The solutions obtained in this study were partitioned over as few as 48 and as many as 200 processors.

Turbulence Modeling: The current UT SimC flow solvers have a wide range of turbulence models including the one-equation Spalart–Allmaras and Menter-SAS models, and the two-equation q–ω and k–ε/k–ω hybrid models. The Spalart–Allmaras turbulence model was initially used in this study. After a brief numerical study for the first test case comparing the results from using the various turbulence models, the two-equation q–ω and k–ε/k–ω hybrid model was selected for use in the remaining cases in this study.

C. Flow Solver Used at Boeing Phantom Works

The Boeing (BCFD) code is a general geometry and general purpose Euler and Navier–Stokes solver [26]. BCFD supports multiblock grids containing any combination of structured or unstructured blocks (zones). For this study, only unstructured blocks were used. The unstructured blocks can contain any mixture of tet, hex, prism, and pyramid elements. A mature second-order accurate zone coupling technique ensures continuity of the solution across zone boundaries. BCFD has an extensive library of boundary condition routines available on a point-by-point basis as well as various spatial algorithms such as Roe, Harten, van Leer, Lax, and Enfield (HLLE), and Lax–Freidrichs/Rusanov. The default spatial operator is a finite-volume second-order HLLE flux-difference split scheme. Gradient reconstruction is performed at the cell centers and uses a total variation diminishing limiter to improve robustness and convergence rate. Turbulence models implemented in BCFD include the one-equation pointwise model of Goldberg, the one-equation SA model, and the two-equation Menter SST model. Also, the hybrid (RANS-LES) models SA/DES, SA/Shin's modified DES model, and SST/large eddy stress balance, partially resolved numerical simulation (PRNS), and detached PRNS have been implemented.

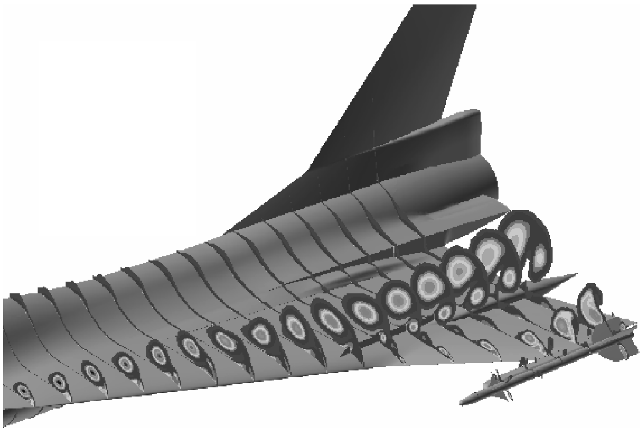

Fig. 4 Vortical structure of flowfield for FC 7 ($M_\infty = 0.304$, $\alpha = 11.89$ deg, and $Re = 44.4$ M, Boeing result).

BCFD incorporates a number of user-selectable (by zone) solution algorithms. The default time integration scheme is a first-order, implicit scheme where a point Gauss–Seidel with agglomeration multigrid is used for unstructured grids. For steady-state flows, variable time steps based on local eigenvalues are used to speed convergence. For time-accurate calculation, BCFD offers a second-order global Newton/dual-time algorithm which provides second-order accurate updates in the physical-time domain across all zones.

D. Flow Solver Used at EADS–MAS

All flow solutions at EADS–MAS were obtained using the DLR flow-solver TAU [14,15]. The TAU code is a software system consisting of several separate modules for the prediction of viscous and inviscid flows about complex geometries employing hybrid unstructured grids. In the actual calculations, the modules for preprocessing (computation of the dual grid, metrics, and connectivity), the flow solver, and the adaptation module have

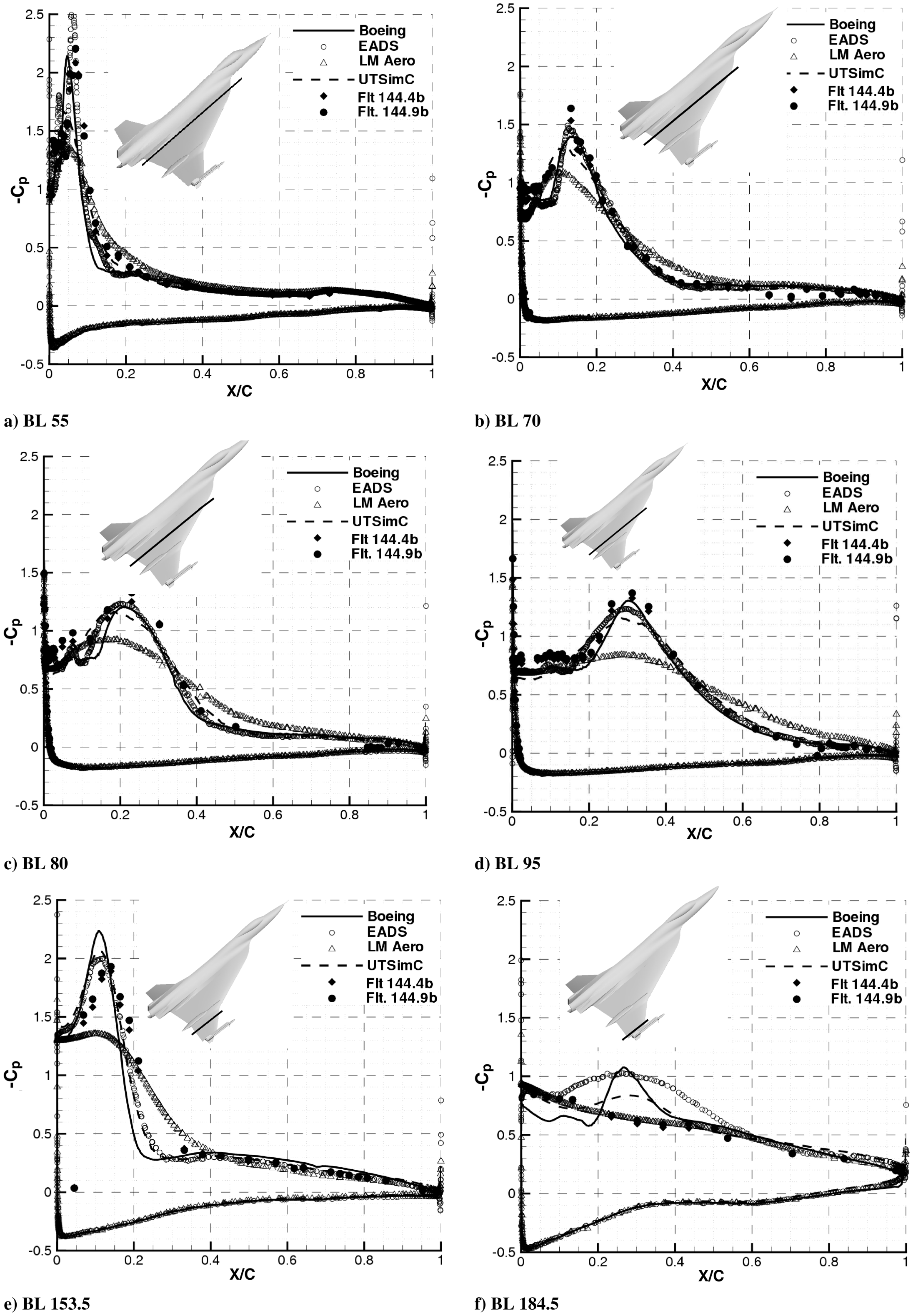

a) BL 55

b) BL 70

c) BL 80

d) BL 95

e) BL 153.5

f) BL 184.5

Fig. 5 Comparison of C_p to flight test data for FC 7 ($M_\infty = 0.304$, $\alpha = 11.89$ deg, and $Re = 44.4$ M) at various butt lines.

been used. The preprocessing had to be run for each new primary grid, that is, also after each adaptation step. The flow-solver module uses an edge-based dual cell approach, where the inviscid terms are computed either by a second-order central scheme or a variety of upwind schemes. For the time integration various explicit Runge–Kutta schemes or the explicit LU-SGS scheme can be employed. Convergence acceleration is achieved by a multigrid algorithm based on agglomerated coarse grids. To allow for turbulence, different one- and two-equation turbulence models as well as DES are available.

In the actual flow calculations, the flow solver was applied with the advection upstream splitting method based on the flux difference and on the flux vector upwind scheme, backward Euler implicit time integration (solved by LU-SGS), Spalart–Allmaras one-equation turbulence model with Edwards modification, and a 3 W multigrid

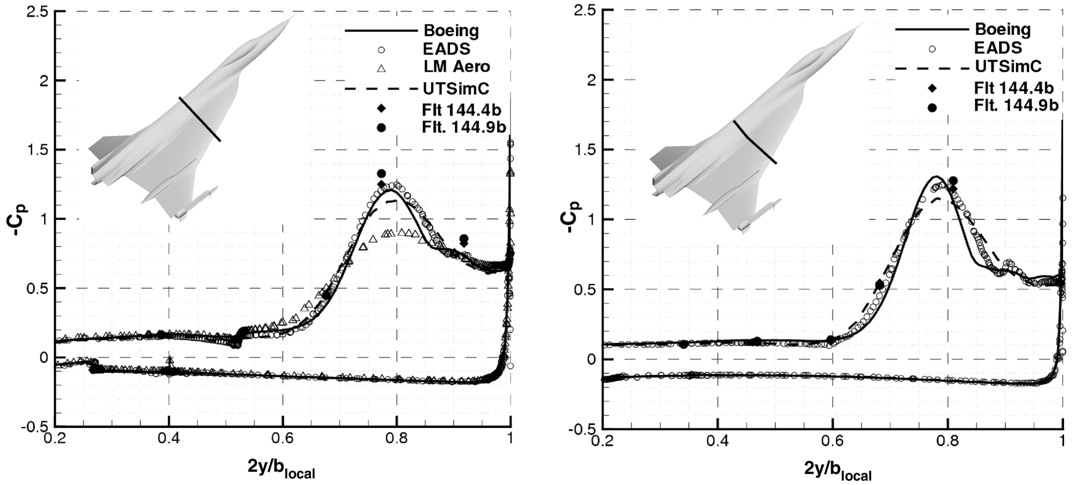

a) FS 300

b) FS 337

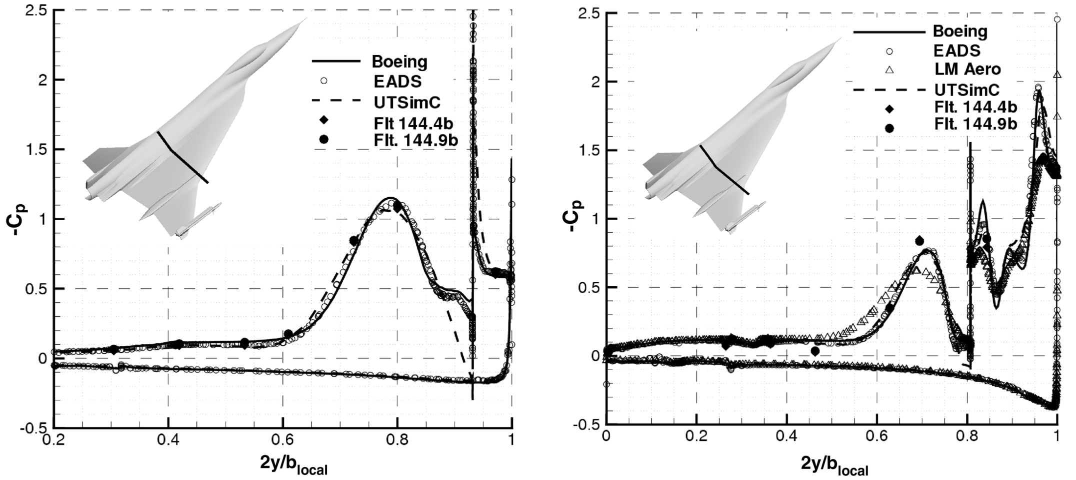

c) FS 375

d) FS 407

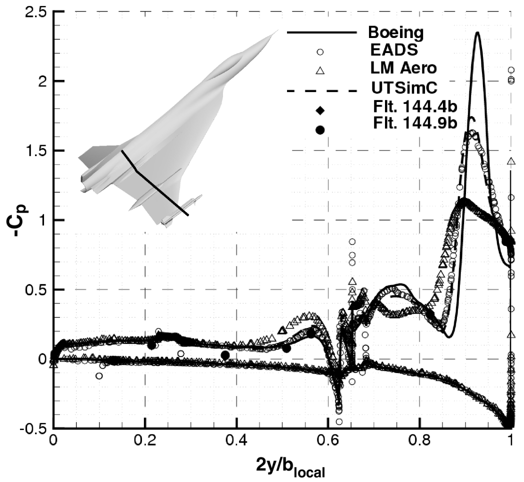

e) FS 450

Fig. 6 Comparison of C_p to flight test data for FC 7 ($M_\infty = 0.304$, $\alpha = 11.89$ deg, and $Re = 44.4$ M) at various fuselage stations.

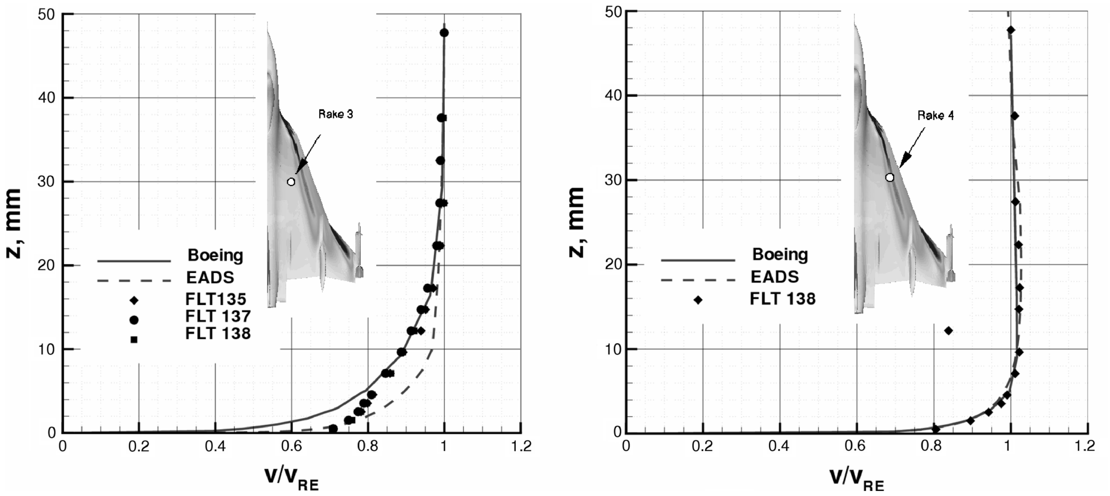

a) Rake 3

b) Rake 4

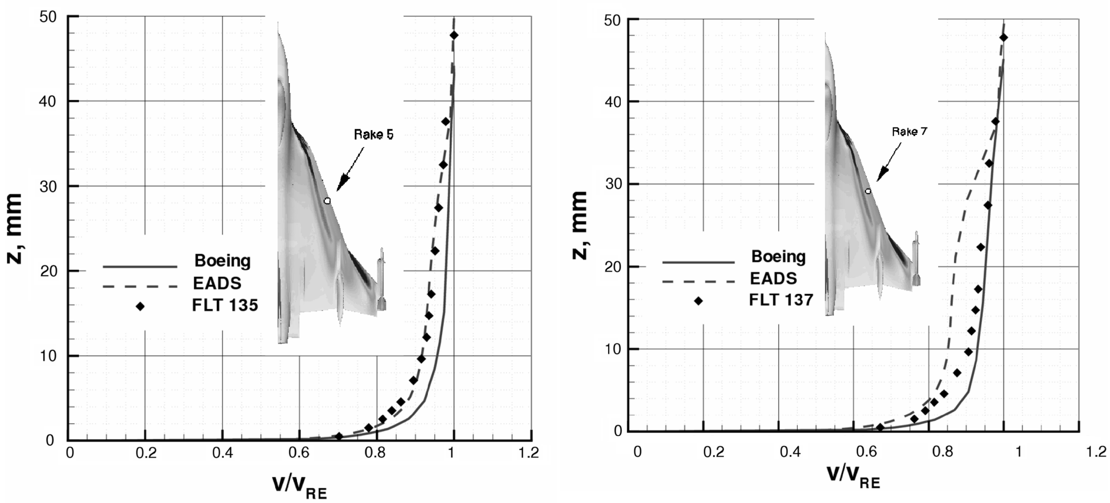

c) Rake 5

d) Rake 7

Fig. 7 Comparison of computed and measured velocity profiles in the upper surface boundary layer of FC 7 ($M_\infty = 0.304$, $\alpha = 11.89$ deg, and $Re = 44.4$ M) at various fuselage stations.

convergence acceleration. For the initial solution 8000 multigrid cycles were run and an additional 4000 cycles after each adaptation step. The flow solutions were run on 32 processors of a 128/2 Linux cluster (2.6 GHz/CPU). This resulted in a CPU time of 13 h per 1000 MG cycles and in a turnaround time of 2–3 weeks for each test case (starting from scratch, four grid adaptations, including all trial and error loops).

Some test calculations using the rotational correction of the turbulence model (SARC) have shown a considerable effect on the eddy viscosity distribution but no effect on the global flow characteristics (pressure distribution, total-pressure distribution, vortical flow structure). Other experiences at EADS–MAS with similar configurations have shown that in fine grids the rotational correction limits the eddy viscosity too much, so that the solution can become unstable and has to be stabilized by high artificial viscosity. For this reason the Spalart–Allmaras Edwards modification and not the SARC turbulence model was used for the calculations.

VI. Results and Discussion

The following sections contain a collection of final results obtained on the different grids. Some more details such as the effects of grid refinement and turbulence models are described in the individual AIAA papers of the authors [10–13]. All experimental data for comparison were taken from the flight test database [2]. The accuracy of the key fight parameters is reported in [2] as ±0.003 for the Mach number at subsonic speeds, ±0.005 for the Mach number at transonic speeds, ±0.3 deg for the angle of attack, and ±0.024 psi for the static pressure over the wing. These accuracy bounds for the Mach number and the static pressure result in

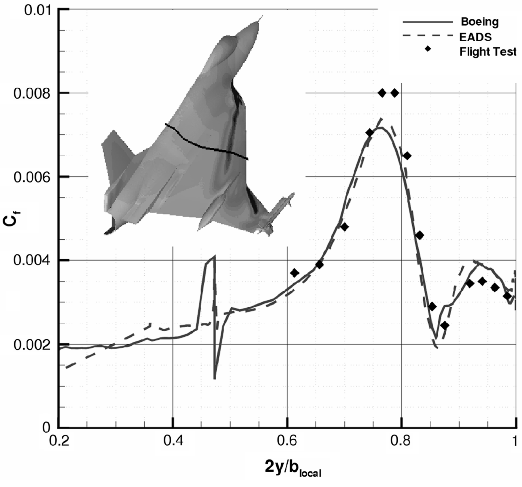

Fig. 8 Comparison of computed and measured values of the magnitude of C_f at FS 330 at FC 19 ($M_\infty = 0.36, \alpha = 11.85$ deg, and $Re = 46.8$ M) at various fuselage stations.

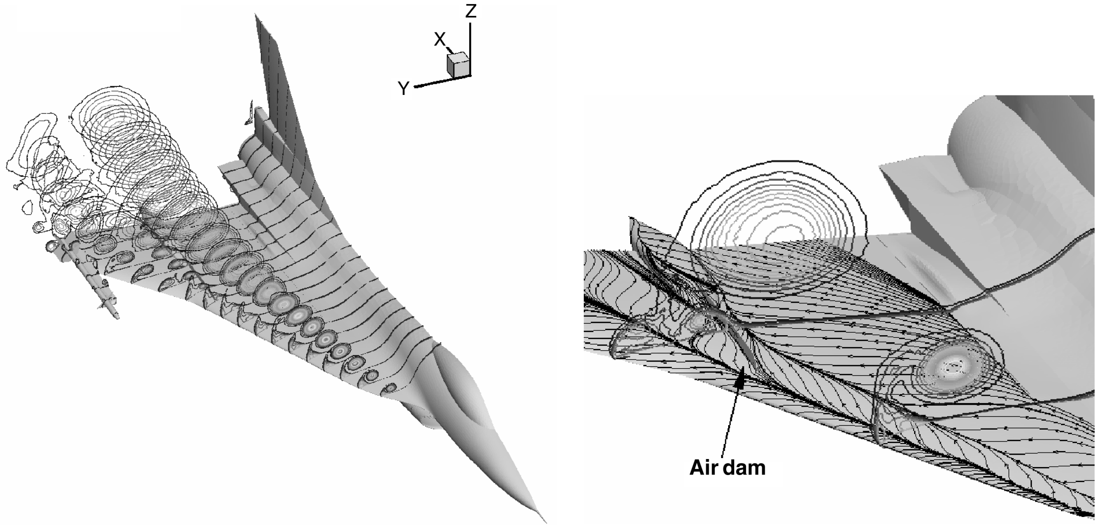

a) Total-pressure loss contours **b) Surface skin friction lines**

Fig. 9 Vortical structure of flowfield for FC 25 ($M_\infty = 0.242$, $\alpha = 19.8$ deg, and $Re = 32.22$ M) by spanwise contours of total-pressure loss (EADS result).

maximum error bars for the c_p values of $\Delta c_p \pm 0.1$ at $M_\infty = 0.242$, and $\Delta c_p \pm 0.01$ at $M_\infty = 0.97$.

A. Influence of the Grid Adaptation on Pressure Distribution and Vortex Location

In the case of 3-D CFD simulations about complex configurations there is always the question about the sensitivity of the results to the grids used. The use of solution adaptive grids can help to investigate this sensitivity and can give an indication about the grid convergence of the solution. This effect of the grid adaptation is shown in Figs. 2 and 3 for FC 25 ($M_\infty = 0.242$, $\alpha = 19.8$ deg, and $Re = 32.22$ M) This flight condition features the highest angle of attack and by this the most distinctive leading-edge vortices. Both figures illustrate the convergence of the surface pressures during the four adaptation steps toward a final pressure distribution. There is hardly any difference between the result of the third adaptation step and the fourth adaptation step. So it can be concluded that the results after the fourth adaptation step can be considered as final results.

The location and the strength of the leading-edge vortex also changes during the adaptation. In the coarse grids, the location of the leading-edge vortex is too far upstream and the leeward suction peak is clearly underpredicted. During the adaptation the location of the vortex moves more downstream (Fig. 2) and it becomes more distinct. Also the secondary vortex becomes more distinct during the adaptation.

B. FC 7: $M_\infty = 0.304$, $\alpha = 11.89$ deg, and $Re = 44.4$ M

Flight condition 7 is a case of fully developed, subsonic vortical flow over the upper surface without vortex breakdown before the trailing edge. Figure 4 shows the vortical structure of the flowfield in terms of total-pressure contours (Boeing result). The flowfield is characterized by three primary vortices. The largest vortex forms at the root of the wing fuselage intersection (where the wing has a sharp leading edge) and is fed by the flow around the 70 deg sweep inboard wing leading edge. Beneath this big leading-edge vortex there forms a typical secondary vortex with opposite sense of rotation. About halfway between the wing root and tip, the leading-edge sweep suddenly changes to a sweep angle of 50 deg. At this crank in the leading-edge sweep, a second primary vortex is formed and there is also an additional secondary vortex. Just inboard of the wing crank, there is a large vertical plate (fence) that limits communication between the inboard and outboard portions of the wing. A third primary vortex is generated at the leading edge of the fence and tracks on the outboard portion of the wing. Interactions between the inboard wing vortex and the fence play an important role in establishing the flowfield.

Figure 5 presents comparisons of the computed and flight-tested surface pressure coefficients plotted along the butt lines (BL). The development of the primary vortex begins at the (sharp) leading edge at BL 55 (Fig. 5a). This can be seen in the very compact suction peak of the upper surface pressure distribution. In the EADS solution, this suction peak is at the correct position, but its value is overpredicted. There is also a distinctive secondary vortex peak in the EADS result. The Boeing solution predicts nearly exactly the magnitude of the suction peak, but its position is slightly more upstream. In the UT SimC and LM Aero solutions the magnitude of the leading-edge suction peak is underpredicted. At BL 70 (Fig. 5b) the solutions of Boeing and EADS are very close and both solutions show very clearly the effect of a secondary vortex. More outboard, at BL 80, BL 95, and BL 153.5 (Figs. 5c–5e), the solutions of Boeing, EADS, and UT SimC are very close and they are all in good agreement with the flight test data. Only the LM Aero solution shows a clear underprediction of the leeward suction peak. It seems that the primary vortex is represented too weak in the LM Aero simulation. It was thought that a possible reason for this effect may be the compression factor setting for the flux limiter in the LM Aero flow solver [12]. Increasing the compression factor increased the suction peak slightly, but not nearly enough to match flight test data. The inadequacy of the wall function approach for this problem is believed to be the reason that the suction peak is underpredicted. The suction peak at BL 153.5 (Fig. 5e) is due to the outer primary vortex, which is generated by the crank in the wing leading edge. At the outer wing section BL 184.5 (Fig. 5f), the footprint of this vortex can be seen very clearly in the EADS solution. There is also an effect of this vortex in the Boeing solution and a very weak effect in the UT SimC solution. The LM Aero results show no effect of such a vortex and thus agree very well with the flight test data, which also show no effect of a vortex. As all grids are adapted or refined in this region, the different effects of this outboard vortex may be related to the different turbulence models.

Figure 6 shows the surface pressure distributions in different “fuselage stations” (FS). This representation gives better insight into the vortical flow structure. At FS 300 (Fig. 6a) all solutions show the effect of a secondary vortex and all solutions predict the primary vortex at about 80% span, which is in good agreement with the few flight test data points. The LM Aero results show again the above-mentioned underprediction of the primary vortex suction peak. The other three solutions show only small differences, which may be related to the different turbulence models. At FS 375 the main feature is the effect of the air dam (Fig. 6c). The results of Boeing, EADS, and UT SimC are more or less identical in this section. At FS 407 (Fig. 6d) and FS 450 (Fig. 6e) there are some substantial differences in the results for the air-dam vortex peak, the flow over the actuator pod, and the outer wing vortex.

Figure 7 shows the boundary-layer comparison between the measured and predicted data at four different positions (v_e is the velocity at the rake extreme total-pressure tube). Rake 3 (Fig. 7a) is inboard of the primary vortex and should be in a basically streamwise flow. Here the EADS results show more full profiles indicating a higher turbulence level than in the experimental data. Rake 4 is beneath the primary vortex (Fig. 7b) and the agreement of both numerical results with the flight test data is pretty good. Rakes 5 and 7 are both outboard of the primary vortex and very close to each other. At both rakes the Boeing results now show slightly fuller profiles compared to the flight test data. Although for rake 5 the EADS results show very good agreement with the flight test data, there is a considerable defect in the velocity profiles at rake 7.

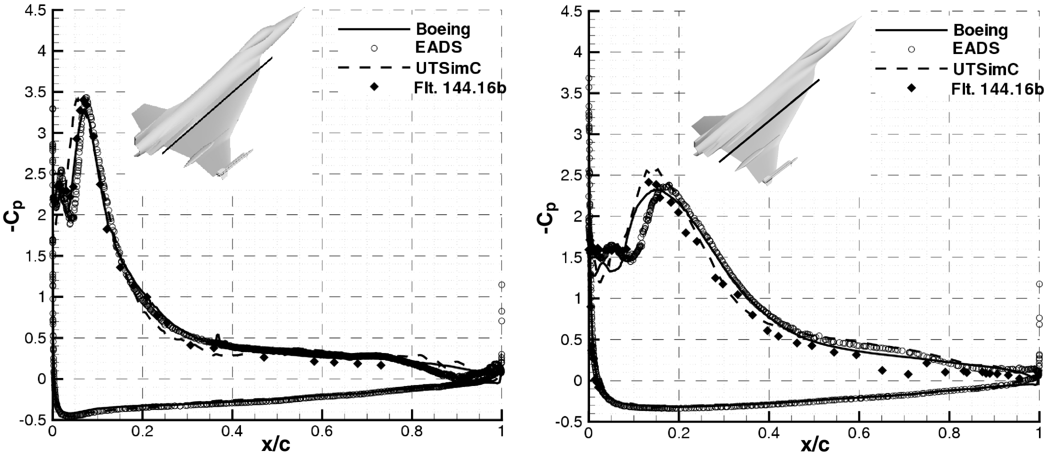

a) BL 55

b) BL 70

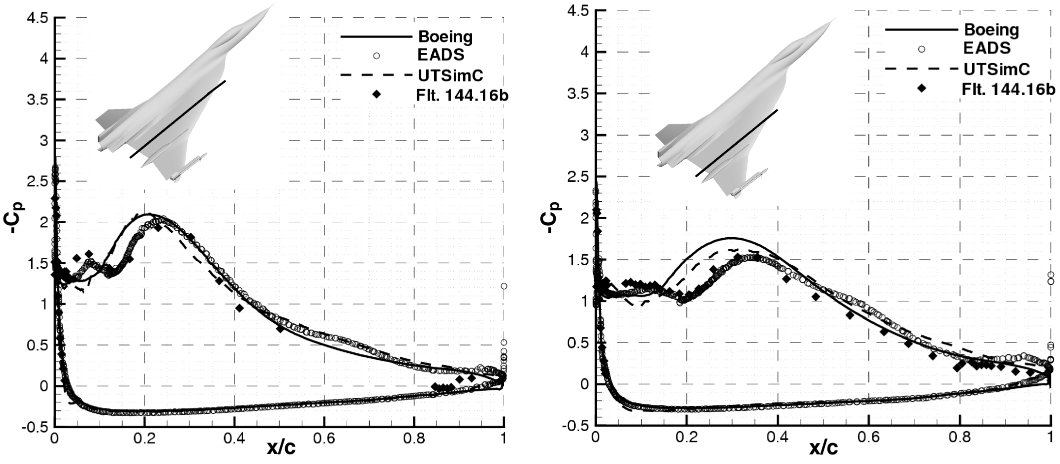

c) BL 80

d) BL 95

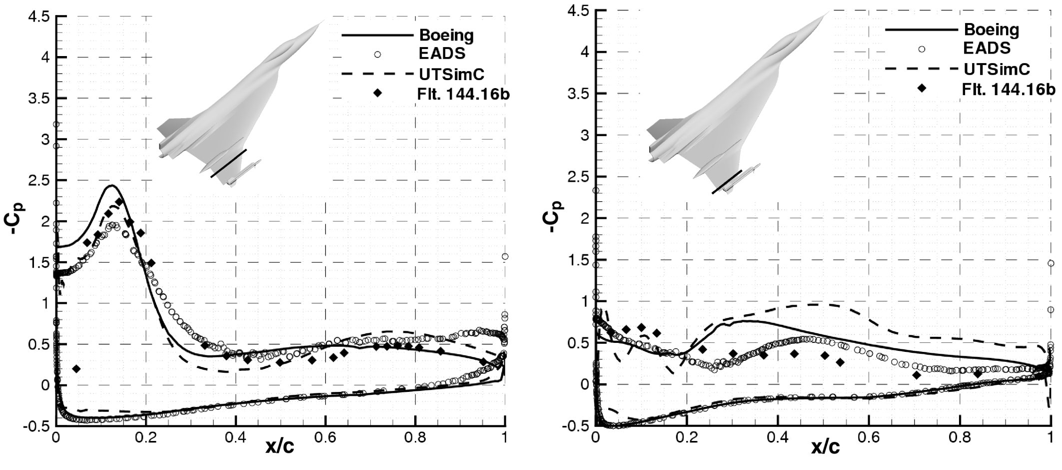

e) BL 153.5

f) BL 184.5

Fig. 10 Comparison of C_p to flight test data for FC 25 ($M_\infty = 0.242$, $\alpha = 19.8$ deg, and $Re = 32.22$ M) at various butt lines.

C. FC 19: $M_\infty = 0.360$, $\alpha = 11.85$ deg, and $Re = 46.8$ M

Flight condition 19 is also a case of fully developed vortical flow over the upper surface without vortex breakdown before the trailing edge and the vortical flowfield is very similar to that of FC 7. For this flight condition flight test measurements of the skin friction coefficient C_f at FS 330 were available. Figure 8 compares the computed and measured skin friction coefficient at FS 330.

There are two peaks in the skin friction distribution. The smaller one, close to the leading edge, indicates the presence of a secondary vortex and the higher one indicates the presence of a primary vortex above the surface. Figure 8 presents the numerical results of Boeing and EADS. Both results are very close, and both results show a jump at 45% span, which is caused by a step in the geometry. The level associated with the primary vortex is not exactly reached by the

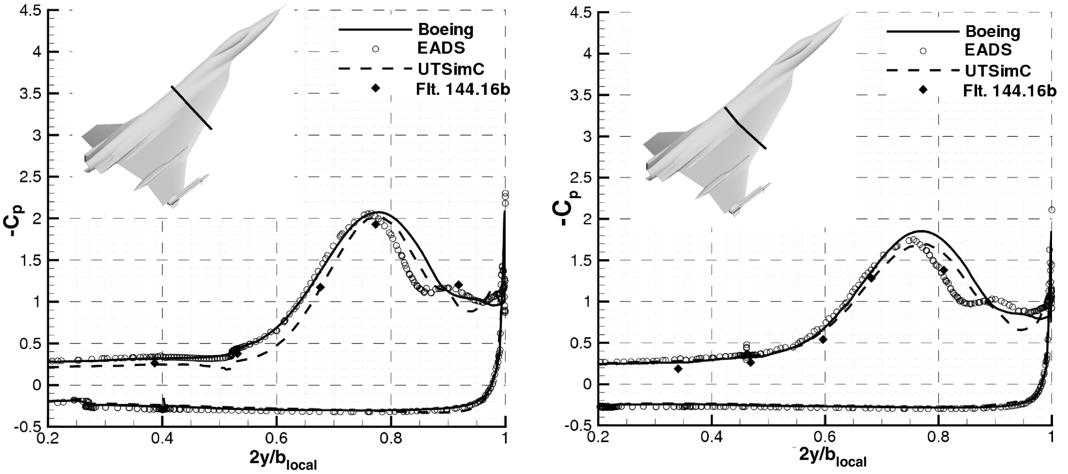

a) FS 300

b) FS 337

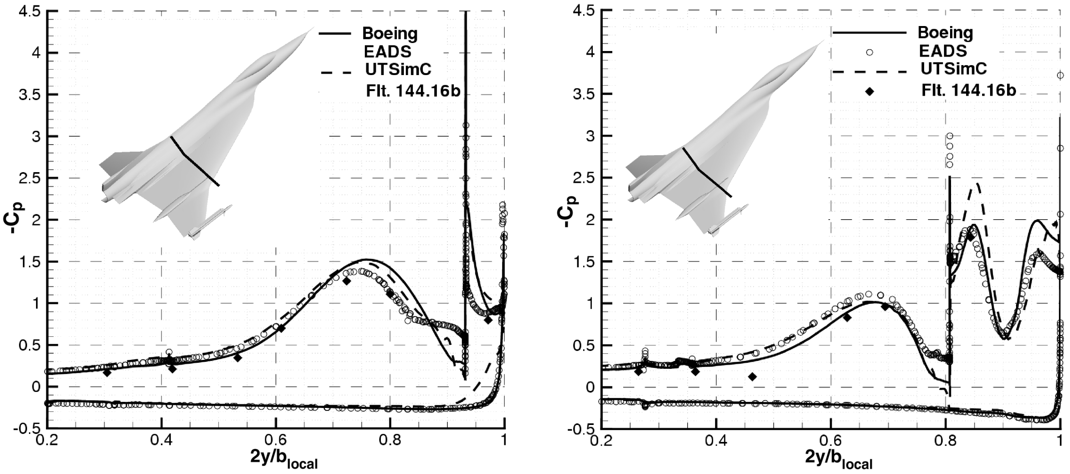

c) FS 375

d) FS 407

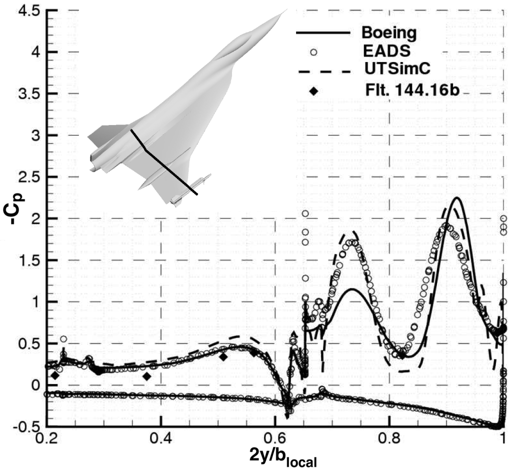

e) FS 450

Fig. 11 Comparison of C_p to flight test data for FC 25 ($M_\infty = 0.242$, $\alpha = 19.8$ deg, and $Re = 32.22$ M) at various fuselage stations.

calculations, but the spanwise location is perfectly matched. The second peak is slightly overpredicted.

D. FC 25: $M_\infty = 0.242$, $\alpha = 19.84$ deg, and $Re = 32.22$ M

Flight condition 25 is characterized by much stronger vortices and by possible vortex breakdown over the rear end of the wing. There is more unsteadiness in the flowfield and hence this test case may be a very challenging or even overstraining test case for steady RANS calculations. Figure 9 shows the vortical flowfield by means of contours of total-pressure loss (Fig. 9a) and upper surface skin friction lines (Fig. 9b).

At the apex of the wing a primary vortex develops, which moves inboard and upward of the wing when going in the streamwise direction. As the vortex core moves away from the leading edge, the affect on the vortex by the leading edge becomes weaker and weaker (this can be seen by the decreasing total-pressure loss in the vortex core). Beginning at the air dam, the primary vortex loses the connection to the leading edge and is no longer fed by it. If this main primary vortex undergoes vortex breakdown, then it must happen in this rearward region of the wing. (A simple 70-deg swept delta wing usually has no vortex breakdown at $\alpha = 20$ deg.) Figure 9a does not clearly indicate whether there is vortex breakdown or not. At best there is a very small bubble-type vortex breakdown region at the rear end of the wing. This may also be due to the limitations of RANS, as, for example, DES simulations of Morton et al. [9], indicate vortex breakdown more clearly.

Because of the side wash of the primary vortex, there is outboard directed flow at the air dam, which crosses it and induces a new vortex, which turns in the opposite direction of the wing primary vortex. At the crank, the sharp leading edge of the outer wing induces a new primary vortex, which turns in the same direction as the wing primary vortex. Upstream of the air dam there is a secondary vortex beneath the primary vortex. Between the secondary vortex and the wing leading edge, there is another vortex. It has the same rotational direction as the primary vortex and can be considered as an elementary part of the feeding sheet of this primary vortex. Rearward of the wing, the air-dam vortex, the outboard wing leading-edge vortex, and the missile induced vortices merge into one common vortex.

Figure 9b shows more details of the flow structure at the air dam and at the actuator pod. Upstream of the air dam, the primary vortex and the secondary vortex, as well as the small vortex between the secondary vortex and the leading edge with their separation and attachment lines, can be found very clearly in the skin friction lines. Figure 9b also shows the interaction of the secondary vortex with the air dam more detailed. The air dam divides the secondary vortex into a small outboard part and into a main part, which remains inboard of the air dam. The outboard part merges into the air-dam vortex, whereas the inboard part serves the outboard directed flow as a ramp to ease the crossing of the air dam.

Similar to FC 7, Figs. 10 and 11 present comparisons of computed and flight-tested surface pressure coefficients Cp, plotted along butt lines and fuselage stations. The first four butt lines (Figs. 10a–10d), which are all inside of the air dam, show that the inner wing vortex is being resolved by all three numerical results. As long as there is no effect of the air dam (BL 55, BL 70, and BL 80), there are only small differences in the position of the leeward suction peak and some differences in the region of the secondary vortex. Concerning the secondary vortex, the solution adapted grid of EADS seems to be beneficial. At BL 95 with the beginning of the influence of the air dam and the crank there are some larger differences in the position of the suction peak and in the region of the secondary vortex. The better agreement of the EADS solution may again be related to the solution adapted grid. Outboard of the air dam (BL 153.5, Fig. 10e), all three numerical solutions resolve again the outboard primary vortex and agree pretty good with the flight test data. The small differences between the numerical results may be related to different grid resolutions and different turbulence modeling. At the most outboard station (BL 184.5, Fig. 10f) there is a similar effect as at FC 7: no effect of a vortex in the flight test data, but different effects in the numerical data. This section is strongly affected by the flow about the tip missile and besides grid resolution and turbulence modeling, the additional unsteadiness of the flow may complicate the RANS solution.

The spanwise plots of Cp are presented in Fig. 11. In front of the air dam (FS 300 and FS 337, Figs. 11a and 11b) all three numerical results match the flight test data pretty well. The main difference in the numerical solutions can be related to the effect of the secondary vortex. The EADS result shows a broader secondary vortex than the Boeing and the UTSimC solutions. Thus the suction peak of the EADS solution is more inboard. At the beginning of the air-dam interference (FS 375) all three solutions are very close. In the rearward sections of FS 407 and FS 450 (Figs. 11d and 11e), there is a spreading in the magnitude of the suction peaks of the outer wing vortex, air-dam vortex, and inner wing vortex, but the position of the vortices is the same in all three numerical results.

E. FC 70: $M_\infty = 0.97$, $\alpha = 4.3$ deg, and $Re = 88.8.4$ M

This flight condition is characterized by a high, transonic Mach number, but low incidence. For this test case, transonic flow with embedded shock waves is to be expected, and vortical flow characteristics should be of minor effect.

Figure 12 shows isosurfaces at Mach 1 shaded by total pressure. There are three large sonic surfaces which terminate in very weak shocks. The first starts and terminates on the canopy, the second starts very near the inboard leading edge and terminates at the middle of the inboard wing section, and the third starts roughly at the crank and terminates at the trailing edge. There is a region of smaller sonic surfaces that sit between the second and third large surfaces, which also seem to terminate in very weak shocks. Note also the Mach 1 surfaces at the missile nose, shoulder, and forward fins.

Figure 13 presents computed and flight-tested surface pressure coefficients for this flight condition along butt lines. The comparisons show good agreement at span stations BL 55 (Fig. 13a) and BL 95 Fig. 13d) and poor agreement elsewhere. Especially at the outboard stations BL 153.5 (Fig. 13e) and BL 184.5 (Fig. 13f), there is a large discrepancy between numerical results and flight test data in the nose region of the wing. Possibly there was a leading-edge deflection at the outboard wing during the flight test, which was not included in the CFD model. After the case was computed, it was learned that the flight test data indicated that the outboard leading-edge flap was deflected between 5 and 9 deg upward and the trailing-

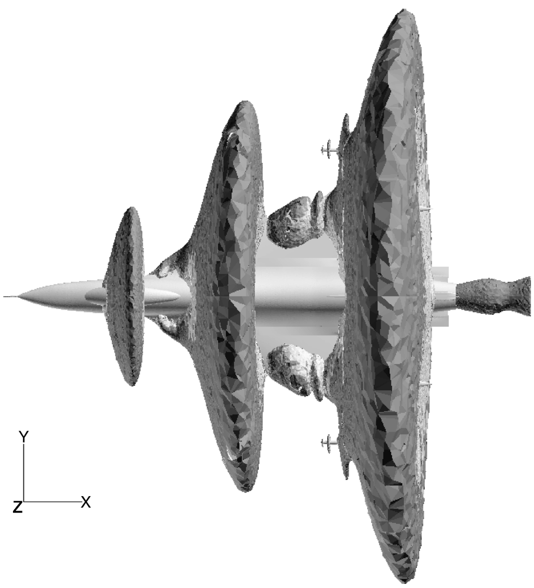

Fig. 12 Shock topology for FC 70 ($M_\infty = 0.97$, $\alpha = 4.3$ deg, and $Re = 88.8$ M). Isosurfaces of Mach 1 are shaded by total pressure showing sonic surfaces and shock waves (LM Aero result).

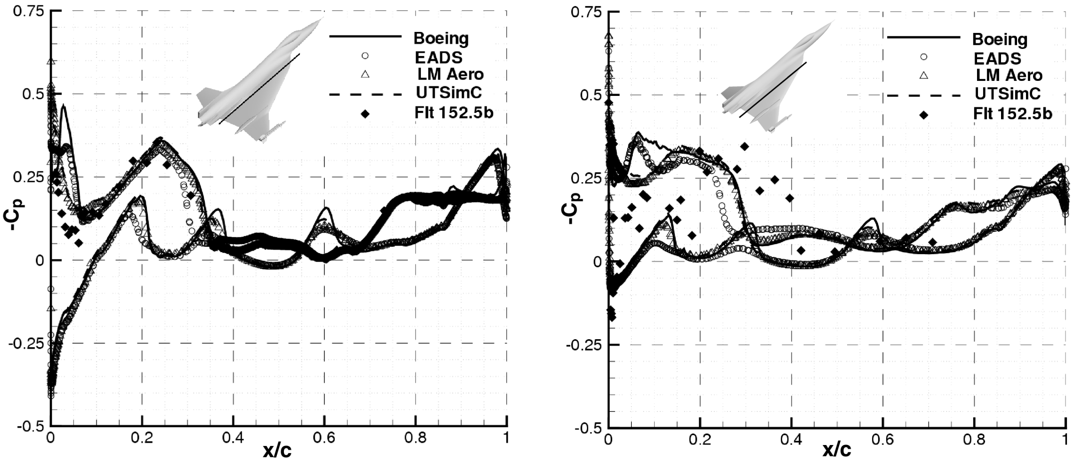

a) BL 55

b) BL 70

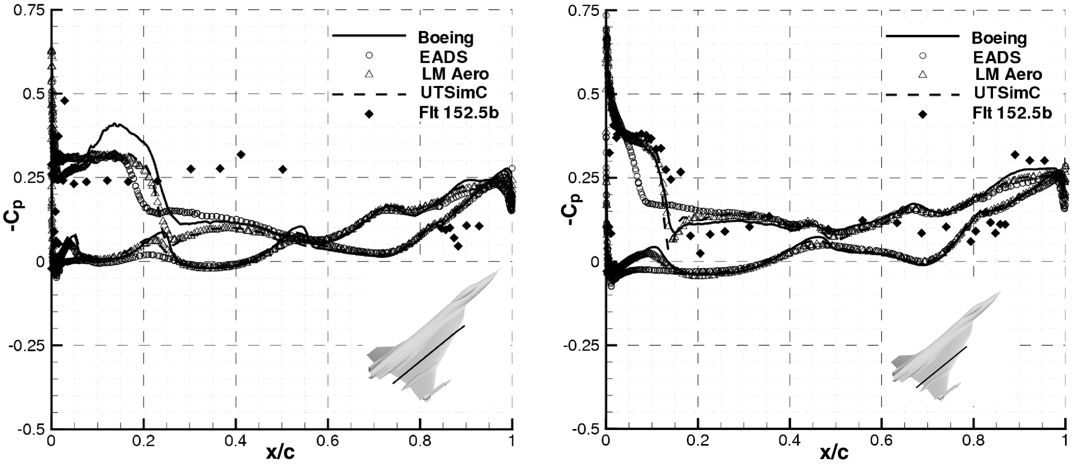

c) BL 80

d) BL 95

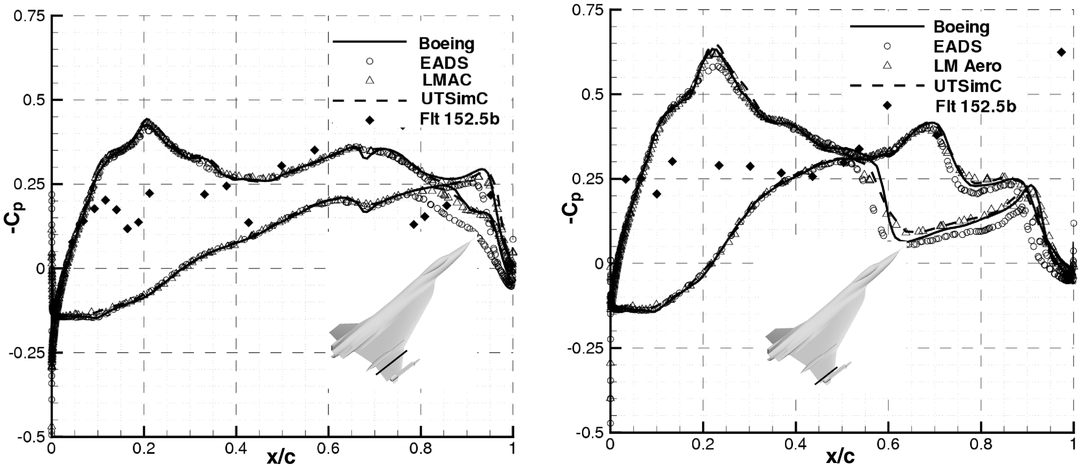

e) BL 153.5

f) BL 184.5

Fig. 13 Comparison of C_p to flight test data for FC 70 ($M_\infty = 0.970$, $\alpha = 4.3$ deg, and $Re = 88.8$ M) at various butt lines.

edge flap about 2 deg downward [2]. The geometry used to create the CFD model did not include leading- or trailing-edge flap deflections. The leading-edge deflection could definitely impact the pressure distribution for the outboard stations. Lamar et al. in [2] indicate that the small trailing-edge deflection could also impact the pressure distribution and the shock location. From examining the flight test data between BL 55 and BL 95 it is hard to understand what physically takes place. These discrepancies also show up in the axial station plots for FS 300, FS 337.5, and FS 375 as shown in Fig. 14.

A comparison of all results of CAWAPI which is given by Rizzi et al. [27] shows the same tendency: the computed data agree very well among themselves but differ substantially from the measurements, except at BL 55 where all results are in good agreement. The results presented in this paper suggest that it cannot be a grid effect, as with all the different grids used here there was the same discrepancy between numerical results and measurements. Additional investigations within the CAWAPI (variation of α, variation of M_∞, small sideslip angles, inviscid calculation) also gave no indication for the reasons of the discrepancy.

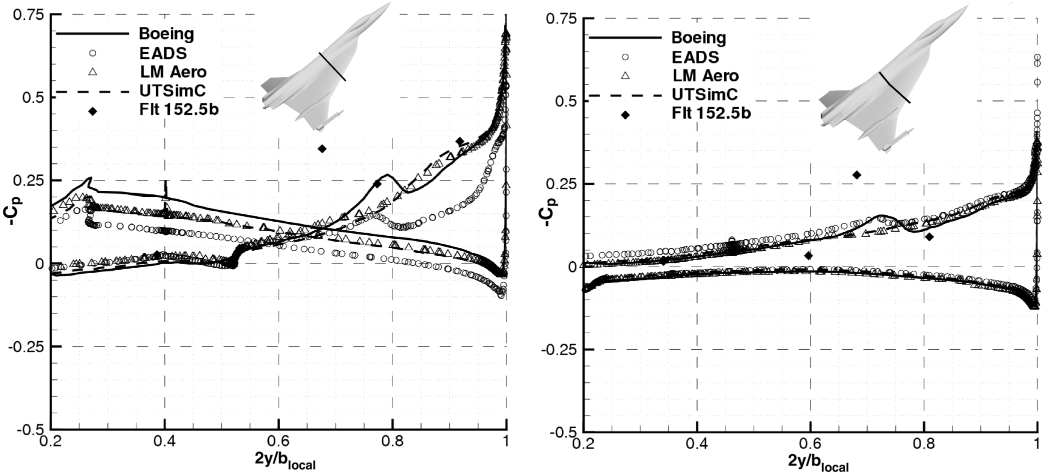

a) FS 300 b) FS 337

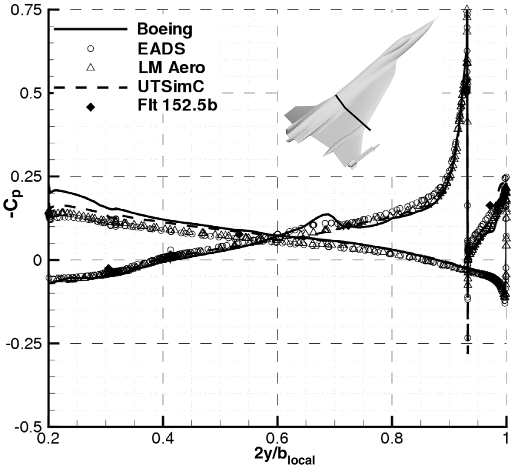

c) FS 375

Fig. 14 Comparison of C_p to flight test data for FC 70 ($M_\infty = 0.970$, $\alpha = 4.3$ deg, and $Re = 88.8$ M) at various fuselage stations.

VII. Conclusions

Given the complex nature of the flowfield, most of the CFD predictions presented in this paper demonstrate that flowfield data measured on the F-16XL fighter aircraft can be predicted by CFD. The presented results underlie the fact that essential data such as pressure distribution, velocity profiles, and skin friction coefficients can be predicted within a satisfactory accuracy (except for FC 70). With a pretty good agreement of those global data, it can also be concluded that the 3-D behavior of the flowfield can be predicted correctly by the CFD tools of today.

It was seen that mesh resolution is critically important in accurately computing viscous vortical flowfields. As grid-independent RANS solutions with globally refined hybrid grids are not possible in an industrial environment, the authors applied different adaptation techniques to minimize the grid dependency: refinement of the surface and volume grid in critical regions (UTSimC), additional adaptation of the volume grid to the flow feature (Boeing), and solution-based surface and volume grid adaptation (EADS). The good agreement of the EADS results for the high alpha test case (FC 25) indicates that the solution-based grid adaptation may be advantageous but it is a very tedious task (several adaptation steps during the flow solution, extrapolation of flow solution into new grids, new dual grids, etc.) and requires some experience and several trial and error loops. But on the other hand, the solution-based grid adaptation allows a targeted reduction of grid effects on the solution. In the daily business, however, it is only applied for vortical flow at high angles of attack. At lower incidence the manual adaptation to the flow features as applied by Boeing is a more practical method and often the surface grid refinement of UTSimC is sufficient.

Compared with the other results obtained in CAWAPI (common structured grid, common unstructured grid) it can be stated that the quality of the presented "tuned" grid results is of the same quality as the results obtained in the common unstructured grid, but that the grid dependency of the results has been reduced. It was not possible to overcome the discrepancy between numerical results and experimental surface pressure distribution at FC 70 by the use of individually tuned grids. So it can be concluded that this discrepancy is not a grid effect.

Acknowledgments

The authors thank all the members of the North Atlantic Treaty Organization–Research and Technology Organization (NATO-RTO) task group AVT-113 "Understanding and Modeling Vortical Flows to Improve the Technology Readiness Level for Military Aircraft" and particularly J. E. Lamar and D. Hummel for their contributions during the course of this project.

References

[1] Lamar, J. E., and Obara, C. J., "Review of Cranked-Arrow Wing Aerodynamics Project: Its International Aeronautical Community Role," AIAA Paper 2007-487, 2007.

[2] Lamar, J. E., Obara, C. J., Fisher, B. D., and Fisher, D. F., "Flight, Wind-Tunnel and Computational Fluid Dynamics Comparison for Cranked Arrow Wing (F-16XL-I) at Subsonic and Transonic Speeds," NASA

TP-2001-210629, 2001.

[3] Boelens, O. J., Goertz, S., Morton, S., Fritz, W., Karman, S. I., Jr., Michal, T., and Lamar, J. E., "Description of the F-16XL Geometry and Computational Grids Used in Cawapi," *Journal of Aircraft*, Vol. 46, No. 2, 2009, pp. 369–376. doi:10.2514/1.34852

[4] Boelens, O. J., Spekreijse, S. P., Systma, H. A., and de Cock, K. M. J., "Comparison of Measured and Simulated Flow Features for the Full-Scale F-16XL Aircraft," AIAA Paper 2007-0489, 2007.

[5] Badcock, K. J., "Evaluation of Results from a Reynolds Averaged Multiblock Code Against F-16XL Flight Data," AIAA Paper 2007-0490, 2007.

[6] Elmiligue, A. A., Abdol-Hamid, K. S., and Massey, S. J., "PAB3D Simulations for the CAWAPI F-16XL," AIAA Paper 2007-0491, 2007.

[7] Goertz, S., and Jirasek, A., "Unstructured Steady/Unsteady Solutions with Edge for CAWAPI F-16XL at KTH/FOI," AIAA Paper 2007-0678, 2007.

[8] Lamar, J. E., and Abdol-Hamid, K. S., "USM3D Unstructured Grid Solutions for CAWAPI at NASA LaRC," AIAA Paper 2007-0682, 2007.

[9] Morton, S. A., McDaniels, D. R., and Cumming, R. M., "F-16XL Unsteady Simulations for the CAWAPI F-16XL Facet of RTO Task Group AVT-113," AIAA Paper 2007-0493, 2007.

[10] Michal, T., Oser, M., Mani, M., and Ross, F., "BCFD Unstructured-Grid Predictions On The F-16XL (CAWAPI) Aircraft," AIAA Paper 2007-0679, 2007.

[11] Fritz, W., "RANS Solutions for the CAWAPI F-16XL in Solution Adapted Grids," AIAA Paper 2007-0492, 2007.

[12] Davis, M. B., Reed, C., and Yagle, P., "Hybrid Grid Solutions on the (CAWAPI) F-16XL Using Falcon v4," AIAA Paper 2007-0680, 2007.

[13] Karman, S., Michell, B., and Sawyer, S., "Unstructured Grid Solutions of CAWAPI F-16XL by UT SimCenter," AIAA Paper 2007-0681, 2007.

[14] Gerhold, T., Friedrich, O., Evans, J., and Galle, M., "Calculation of Complex Three-Dimensional Configurations Employing the DLR-TAU Code," AIAA Paper 97-0167, 1997.

[15] Schwamborn, D., Gerhold, T., and Kessler, R., "The DLR-TAU Code—An Overview," *ONERA-DLR Aerospace Symposium*, CP ODAS 99, 21–24 June 1999.

[16] Alrutz, T., and Rütten, M., "Investigation of Vortex Breakdown over a Pitching Delta Wing Applying the DLR TAU-Code with Full, Automatic Grid Adaptation," AIAA Paper 2005-5162, 2005.

[17] Roe, P. L., "Characteristic-Based Schemes for the Euler Equations," *Annual Review of Fluid Mechanics*, Vol. 18, 1986, pp. 337–365. doi:10.1146/annurev.fl.18.010186.002005

[18] Smith, B. R., "The *k-kl* Turbulence Model and Wall Layer Model for Compressible Flows," AIAA Paper 90-1483, 1990.

[19] Reed, C. L., Karman, S. L., and Anderson, D. A., "Implementation of Low Speed Preconditioning in the Splitflow Code," AIAA Paper 97-1867, 1997.

[20] Karypis, G., and Kumar, V., "A Fast and High Quality Multilevel Scheme for Partitioning Irregular Graphs," *SIAM Journal on Scientific Computing*, Vol. 20, No. 1, 1998, pp. 359–392. doi:10.1137/S1064827595287997

[21] Anderson, W. K. "Grid Generation and Flow Solution Method for the Euler Equations on UnstructuredGrids," NASA Langley Research Center, TR L-16986, 1992.

[22] Anderson, W. K., and Bonhaus, D. L., "An Implicit Upwind Algorithm for Computing Turbulent Flows on Unstructured Grids," *Computers in Fluids*, Vol. 23, No. 1, 1994, pp. 1–21.

[23] Anderson, W. K., Rausch, R. D., and Bonhaus, D. L., "Implicit/Multigrid Algorithms for IncompressibleTurbulent Flows on Unstructured Grids," AIAA Paper 95-1740, 1995.

[24] Hyams, D. G., Sreenivas, K., Sheng, C., Briley, W. R., Marcum, D. L., and Whitfield, D. L., "An Investigation of Parallel Implicit Solution Algorithms for Incompressible Flows on Multielement Unstructured Topologies," AIAA Paper 2000-0271, 2007.

[25] Briley, W. R., Taylor, L. K., and Whitfield, D. L., "High Resolution Viscous Flow Simulations at Arbitrary Mach Number," *Journal of Computational Physics*, Vol. 184, No. 1, 2003, pp. 79–105. doi:10.1016/S0021-9991(02)00018-9

[26] Mani, M., Cary, A., and Ramakrishnan, S. V., "A Structured and Hybrid Unstructured Grid Euler and Navier-Stokes Solver for General Geometry," AIAA Paper 2004 524, 2004.

[27] Rizzi, A., Badcock, K., Jirasek, A., and Boelens, O., "What Was Learned from Numerical Simulations of F-16XL (CAWAPI) at Flight Conditions," AIAA Paper 2007-0683, 2007.